






Article

New Bi-Nuclear Nickel(II) Complex-Based Salen Schiff Base: Synthesis, Crystal Structure, Spectroscopic, Thermal, and Electrical Investigations

Bouchra Es-Sounni ¹, El Mehdi Haily ² , Asmae Nakkabi ³, Mohamed Bakhouch ^{4,*} , Linda Bejaoui ⁵, Savaş Kaya ⁶, Mohamed El Yazidi ³ , Lahcen Bih ⁷, Mohamed Saadi ⁸ , Lahcen El Ammari ⁸  and Mohammed Fahim ^{1,*}

- ¹ Laboratory of Innovative Materials and Biotechnology of Naturel Resources, Faculty of Sciences, Moulay Ismail University, P.O. Box 11201, Meknes 50000, Morocco
- ² Composites and Nanocomposites Center, Moroccan Foundation for Advanced Science, Innovation and Research (MAScIR), Rabat Design Center, Rabat 10100, Morocco
- ³ Engineering Laboratory of Organometallic and Molecular Materials and Environment, Faculty of Sciences Dhar EL Mahraz, University Sidi Mohamed Ben Abdellah, P.O. Box 1796, Fez 30000, Morocco
- ⁴ Laboratory of Bioorganic Chemistry, Department of Chemistry, Faculty of Sciences, Chouaib Doukkali University, P.O. Box 24, El Jadida 24000, Morocco
- ⁵ Unité de Recherche de Chimie des Matériaux et de l'Environnement (UR11ES25), ISSBAT, Université de Tunis El Manar, 9, Avenue Dr. Zoheir Safi, Tunis 1006, Tunisia
- ⁶ Department of Pharmacy, Health Services Vocational School, Sivas Cumhuriyet University, 58140 Sivas, Turkey
- ⁷ Laboratoire des Sciences et Métiers de L'Ingénieur (LSMI), Département Matériaux et Procédés, ENSAM Meknès, Université Moulay Ismail, Meknes 50500, Morocco
- ⁸ Laboratoire de Chimie Appliquée des Matériaux, Centres des Sciences des Matériaux, Faculty of Science, Mohammed V University in Rabat, Avenue Ibn Battouta, BP. 1014, Rabat 10096, Morocco
- * Correspondence: bakhouch.m@ucd.ac.ma (M.B.); mo.fahim@yahoo.fr (M.F.)



Citation: Es-Sounni, B.; Haily, E.M.; Nakkabi, A.; Bakhouch, M.; Bejaoui, L.; Kaya, S.; El Yazidi, M.; Bih, L.; Saadi, M.; El Ammari, L.; et al. New Bi-Nuclear Nickel(II) Complex-Based Salen Schiff Base: Synthesis, Crystal Structure, Spectroscopic, Thermal, and Electrical Investigations. *Chemistry* **2022**, *4*, 1193–1207. <https://doi.org/10.3390/chemistry4040080>

Academic Editors: Małgorzata Hołyńska and Ionut Tranca

Received: 3 September 2022

Accepted: 26 September 2022

Published: 1 October 2022

Publisher's Note: MDPI stays neutral with regard to jurisdictional claims in published maps and institutional affiliations.



Copyright: © 2022 by the authors. Licensee MDPI, Basel, Switzerland. This article is an open access article distributed under the terms and conditions of the Creative Commons Attribution (CC BY) license (<https://creativecommons.org/licenses/by/4.0/>).

Abstract: In this study, a new bi-nuclear nickel complex $[\text{Ni}_2\text{HL}_2(\text{EtOH})_2](\text{Cl})(\text{EtOH})$ of a Schiff base ligand, 2-[3-[2-hydroxybenzylideneamino]propyliminomethyl]phenol, was synthesized and characterized using UV/Vis, IR, HRMS, and TGA/DTA analysis. The molecular structure of the obtained complex was corroborated by the single crystal X-ray diffraction technique. It was found in the complex that two molecules of the ligand coordinate with two nickel atoms through azomethine-N and phenoxy-O, resulting in 6-coordinate distorted octahedral geometry, in which two ethanol molecules occupy the axial positions. The dielectric and electrical properties of the obtained samples were studied by impedance spectroscopy at different frequencies (from 1 Hz to 1 MHz) in the temperature range 298–343 K. It is found that the electrical conductivity of the Ni(II) complex is lower than that of the free ligand H_2L , suggesting that the complexation traps the charge carriers contained in the ligand.

Keywords: Bi-nuclear complex; octahedral geometry; spectroscopy; X-ray crystal structure; Hirshfeld surface analysis; dielectric; conductivity

1. Introduction

Transition metal complexes derived from tetradentate Schiff bases (ONNO) have been extensively studied in virtue of their wide range of applications [1,2]. Indeed, these compounds are known for their anti-corrosion [3], catalytic [4,5], optoelectronic [6,7], electric [8], dielectric [9], magnetic [10,11], and biological properties [12,13].

Many previous studies have found that inorganic metal complexes might exhibit conducting properties [14,15], which are nowadays the subject of a promising research area. Thanks to their useful function in molecular electronics and vital biological life processes, conducting and semiconducting materials have drawn considerable attention [16]. Such

conducting metal complexes stand on the threshold of a bright and exciting future. Hence, the study of the relationship between the chemical structures and electronic characteristics of such compounds still invites further and deeper exploration, as they have a tremendous potential for broader applications that has not been exhausted by their present uses.

Indeed, it is because of this wide range of applications possessed by bi-nuclear metal complexes that they have attracted much interest [17,18]. One of the most attractive properties of bi-nuclear complexes is the interaction exchange possibility between metal centers [19,20]. For they are also known as a catalyst in asymmetric synthesis [21,22], and have a unique catalytic property in the polymerization reaction of olefins compared with mononuclear complexes [23,24]. In addition, they are useful for mimicking bimetallic bio-sites in various proteins and enzymes [25]. Among metal complexes, nickel complexes have attracted great interest in various fields of chemistry [26,27]. Despite that salen and related Schiff's base ligands react with transition metal ions through the deprotonated forms, which act as tetradentate chelating ligand [28,29], some reported works show that the oxygen atoms of the phenoxy groups are not deprotonated [30].

Keeping in view the abovementioned features, we report in this paper the synthesis of undescribed bi-nuclear nickel(II) complex-based 2,2'-((propane-1,3-diylbis(azaneylylidene)) bis(methaneylylidene))diphenol Schiff's base. Spectroscopic studies are performed for the ligand and its corresponding nickel complex to establish their structures and crystallographic studies were used to corroborate the structure of the obtained complex. The dielectric and electrical properties of the obtained compounds were also investigated.

2. Results and Discussion

The salen base Schiff ligand H_2L was prepared by the condensation of propane-1,3-diamine with two equivalents of salicylaldehyde using a common procedure described in the literature [31]. The nickel complex $[Ni_2HL_2(EtOH)_2](Cl)(EtOH)$ was obtained through a simple reaction of a stoichiometric amount of nickel salt ($NiCl_2 \cdot 6H_2O$) with the ligand H_2L in refluxing ethanol.

The schematic representation of the ligand H_2L structure (Figure 1) and its nickel complex $[Ni_2HL_2(EtOH)_2](Cl)(EtOH)$ (Figure 2) was established on the basis of the usual spectroscopic methods, viz.: FT-IR, 1H and ^{13}C NMR, and UV/Vis, as well as mass spectrometry. In addition, the structure of the nickel complex was confirmed by single crystal X-ray diffraction.

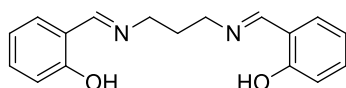


Figure 1. Structure of the ligand H_2L .

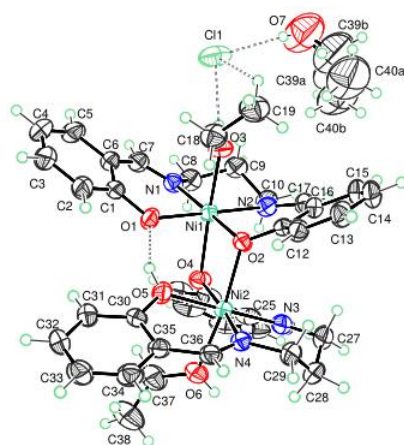


Figure 2. Plot of the $[Ni_2HL_2(EtOH)_2](Cl)(EtOH)$ molecule with the atom-labelling scheme. Displacement ellipsoids are drawn at the 50% probability level. H atoms are represented as small circles.

2.1. Crystal Structure Description

The crystal structure of the title compound is built from two metal ions bound by two organic ligands and two ethanol molecules to form a binuclear nickel(II) complex, in addition to two entity solvents, namely Cl^- and $\text{C}_2\text{H}_5\text{OH}$. The plot of the asymmetric unit of the new dimeric complex, $[\text{Ni}_2\text{HL}_2(\text{EtOH})_2](\text{Cl})(\text{EtOH})$, obtained using the Ortep 3 program [32], is shown in Figure 2. The specificity of the crystal structure of this compound is the disorder at the level of the ethanol solvent molecule. Indeed, the two carbon positions of the ethanol solvent are splitting and the refinement of the occupancy rate of these sites is set to the value obtained after refinement. This refinement requires a constraint on the distances $\text{O7}-\text{C39}(\text{A,B})$ and $\text{C39}(\text{A,B})-\text{C40}(\text{A,B})$. Moreover, there is a void in the structure containing a disordered solvent molecule, which requires the use of SQUEEZE, as implemented in the PLATON and SHELXL programs [33,34].

Furthermore, each nickel atom is surrounded by two nitrogen and two oxygen atoms belonging to one ligand, which build a slightly distorted square plane. In addition, one of the axial positions is occupied by ethanolic oxygen, while the other is filled by oxygen belonging to the second ligand. The resulting Ni coordination polyhedra are two slightly distorted $\text{Ni}_2\text{N}_4\text{O}_6$ edge-sharing octahedra, as shown in Figure 3. As a matter of fact, the $\text{Ni}_2\text{N}_4\text{O}_6$ dimers are linked by hydrogen bonds through solvent molecules, forming chains parallel to the *b* direction with a $\text{Ni1}-\text{Ni2}$ distance between two chelated Ni equal to 3.148 Å, whereas the Ni belonging to neighboring molecules are far apart from each other by ligands. In addition, among the four Schiff base moieties of the title compound, only one (O1N1C1 to C7) is nearly planar, with the largest deviation from planes being $-0.032(3)$ Å at N1 , while the other three ($(\text{O2N2C11}-\text{C17})$, $(\text{O4N3C20}-\text{C26})$, and $(\text{O5N4C30}-\text{C36})$) are inclined with respect to N2 of $0.250(2)$ Å, N3 of $-0.356(3)$ Å, and N4 of $-0.278(3)$ Å, respectively. The two phenyl rings connected to the chelated Ni1 are inclined at $62.12(18)$ to each other and the dihedral angle between the both phenyl cycles linked to Ni2 is $55.92(19)^\circ$.

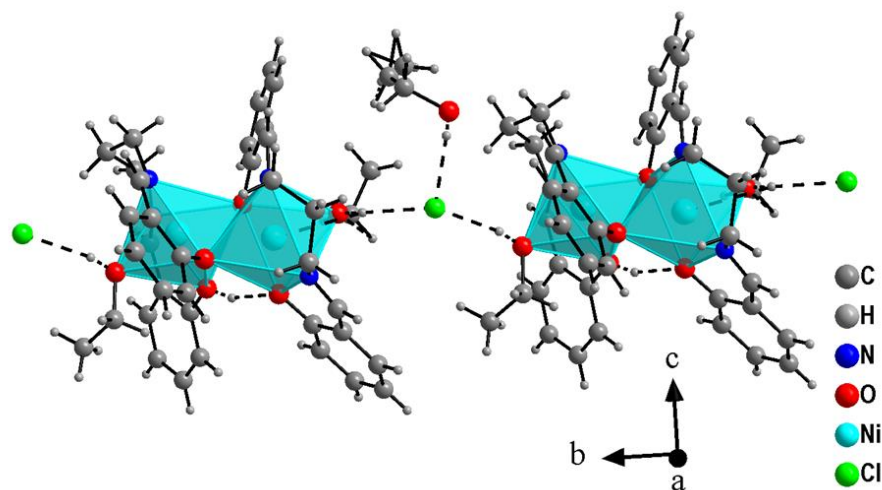


Figure 3. The $\text{Ni}_2\text{N}_4\text{O}_6$ dimers linked by hydrogen bonds through solvent molecules.

In the crystal structure, the molecules are linked together by $\text{O}-\text{H} \cdots \text{Cl}$ hydrogen bonds involving the solvent molecules, namely Cl^- and the free ethanol ($\text{C}_2\text{H}_5\text{OH}$), forming chains parallel to the *b* axis, as shown in Figure 3. These chains are interconnected through $\text{C}-\text{H} \cdots \pi$ interaction between $\text{C8}-\text{H8A}$ and the phenyl ring (C30 to C35). In addition, two other intramolecular $\text{C}-\text{H} \cdots \pi$ interactions are observed in this structure, as shown in Figure 4. Moreover, the complex presents a very strong intramolecular hydrogen bond ($\text{O5}-\text{H50} \cdots \text{O1}$), which forms a bridge between two vertices of the edge-sharing octahedra $\text{Ni}_2\text{N}_4\text{O}_6$ (see Figure 4). The set of $\text{C}-\text{H} \cdots \pi$ interactions and hydrogen bonds are summarized in Table 4.

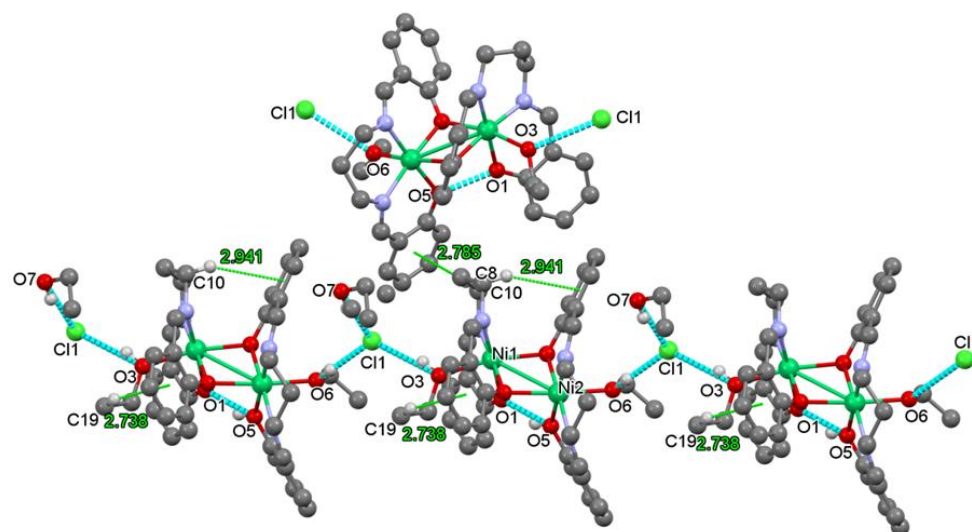


Figure 4. Crystal packing for the $[\text{MHL}_2(\text{EtOH})_2] \cdot (\text{Cl}) \cdot (\text{EtOH})$ showing molecules linked by O–H...Cl hydrogen bonds as dashed blue lines and C–H... π interaction as green lines.

It would be interesting to compare the structure of the present binuclear dimers to those of other Schiff based dimers. Indeed, the structure of the binuclear complex of nickel (II) with Schiff base ligands reported by You et al. [35] is very close to that described in the present work. In both structures, the Ni atoms are in two edge-sharing octahedral sites having a base formed by two imino N atoms and two phenolate O atoms belonging to the Schiff base ligands, while the axial positions are occupied by one ethanol oxygen and one phenolate oxygen, as shown in Figure 2, while in the reported work, the axial positions are filled by one phenolate oxygen and one other oxygen belonging to water or methanol molecules. In the same work, the authors report the structure of the binuclear complex of zinc (II) with Schiff base ligands in which the two zinc atoms are located in a two edge-sharing trigonal-bipyramidal coordination. Moreover, the binuclear centrosymmetric copper (II) complex with the Schiff base $[\text{Cu}(\text{H}_2\text{L})]_2$ displays a distorted square pyramidal geometry surrounding the Cu^{II} [36]. The two copper atoms constituting the dimers are located in the two pyramids sharing a base-apical edge. The Cu–O and Cu–N distances are between 1.9393 (17) Å and 2.010 (2) Å for the square plane and 2.3802(17) Å for the CuO in the axial position. These values are slightly higher than those observed in the monomer complex of copper (II) with the same Schiff base [37]. In this complex, the copper (II) is surrounded by four donor atoms, two oxygen and two nitrogen atoms, forming a distorted square planar geometry. The Cu–O bond lengths are in the range between 1.894(2) and 1.956(2) Å, while the Cu–N distances are between 1.879(3) and 1.997(2) Å for $\text{C}_{22}\text{H}_{20}\text{CuN}_2\text{O}_2$. For more information, a review article on Schiff bases was recently reported by Aragón-Muriel et al. [38] and could be of interest to the authors.

2.2. Spectroscopic Studies

The FT-IR spectra of the ligand H_2L and its corresponding nickel complex are compared to attest the coordination of the ligand. The FT-IR spectrum of the ligand H_2L (Figure S1) reveals in particular the presence of a strong absorption band assigned to the vibration of the (C=N) bond at 1629 cm^{-1} . The absorption band at 3250 cm^{-1} is attributed to the vibration of the (O–H) bond.

On the other hand, the FT-IR spectrum of the nickel complex (Figure S2) shows in particular the presence of a remarkable wideband characteristic of the (O–H) associated bond of the ethanol molecule. Moreover, the stretching vibration of (C=N) was identified at 1622 cm^{-1} , which corroborates the presence of Schiff's base in the complex. Further evidence of chelation of the ligand with the nickel salt was shown by the bands at a

range 444–643 cm^{-1} , assigned to Ni–O and Ni–N vibration in the nickel complex. These assignments are in good agreement with the literature data [39,40].

The proposed structure for the obtained nickel complex was further corroborated using high-resolution mass spectrometry. The mass spectrum recorded in DMSO shows a peak for the protonated molecular ion $[(\text{Ni}_2\text{HL}_2)(\text{Cl})-\text{H}]$ at $m/z = 805.01499$ (Figure S3).

2.3. Electronic Spectra

The absorption spectral data for H_2L and $[\text{Ni}_2\text{HL}_2(\text{EtOH})_2](\text{Cl})(\text{EtOH})$ were obtained in freshly prepared ethanol solution (Figure 5). The ligand H_2L spectrum consists of two relatively intense bands at 264 nm and 295 nm, involving the $\pi \rightarrow \pi^*$ transition, as well as two other low-intensity bands at 354 nm and 440 nm, involving $\pi \rightarrow \pi^*$ excitation of the C=N bond and $n \rightarrow \pi^*$ transition, respectively. Complexation with Ni(II) results in two significant changes of the spectrum. The two intense bands at 279 nm and 298 nm, as well as the relatively low-intensity band at 384 nm shifted to a longer wavelength, witnessed the coordination through azomethine nitrogen (C=N). The band observed at 447 nm could be attributed to the ligand–metal charge transfer transitions. The electronic absorption data of $[\text{Ni}_2\text{HL}_2(\text{EtOH})_2](\text{Cl})(\text{EtOH})$ suggest an octahedral structure [41], which was further confirmed by X-ray crystal structure analysis. The electronic spectral data are listed in Table 1.

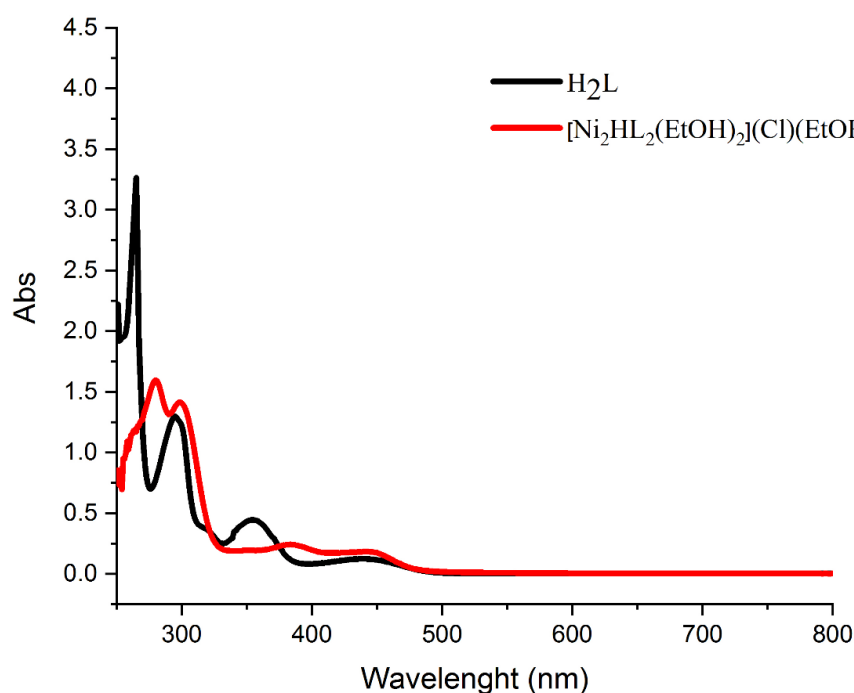


Figure 5. UV/Vis spectra of ligand H_2L and its nickel complex.

Table 1. UV/Vis spectral data for H_2L and $[\text{Ni}_2\text{HL}_2(\text{EtOH})_2](\text{Cl})(\text{EtOH})$.

Entry	Wave Lengths (nm)	Assignment
H_2L	264, 295	$\pi \rightarrow \pi^*$ (phenolic chromophore)
	354	$n \rightarrow \pi^*$
	440	$\pi \rightarrow \pi^*$ (C=N)
$[\text{Ni}_2\text{HL}_2(\text{EtOH})_2](\text{Cl})(\text{EtOH})$	279, 298	$\pi \rightarrow \pi^*$
	384	$n \rightarrow \pi^*$
	447	$d \rightarrow \pi^*$ charge transfer (CT)

2.4. Thermogravimetric Analysis

The purity and thermal stability of the free ligand H_2L and its nickel complex $[Ni_2HL_2(EtOH)_2](Cl)(EtOH)$ were investigated by thermal gravimetric analysis (TGA) and differential thermal analysis (DTA) in the range of 0 to 600 °C and heating rate of 10 °C per minute in an open atmosphere. The free ligand H_2L reflected acceptable stability up to 200 °C, then started to decompose in a single step up to Toff ~ 228 °C and TDTA = 300 °C. The volatilized mass represents about 46%, which corresponds to the loss of nearly $2H_2O$, $2NH_3$, and $5(CO \text{ or } CO_2)$, as shown in Figure 6.

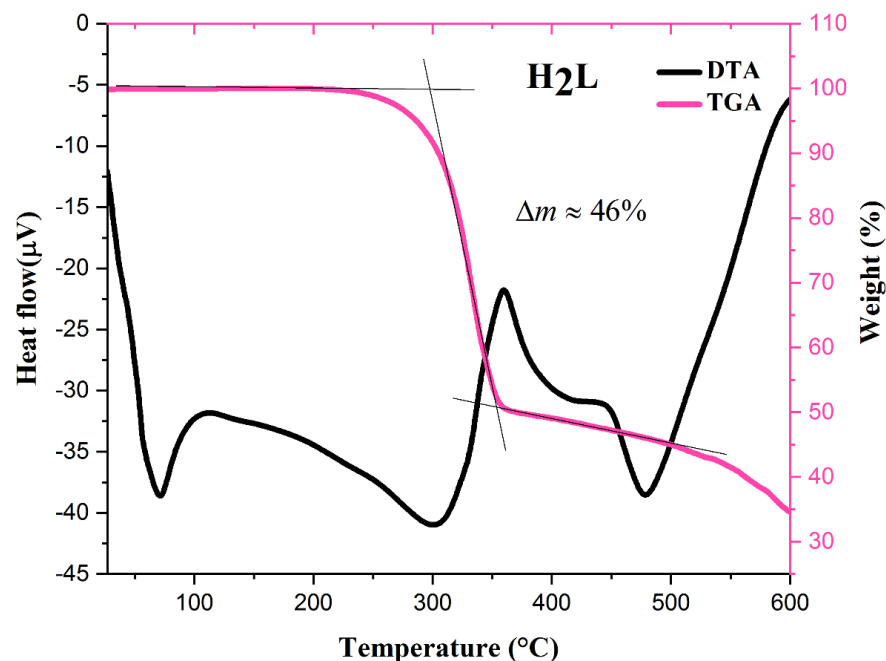


Figure 6. TGA and DTA of the free ligand H_2L .

However, the complex $[Ni_2HL_2(EtOH)_2](Cl)(EtOH)$ showed a completely different decomposition pattern with two distinct pyrolysis steps (Figure 7). The first decomposition step was recorded between 90 and 143 °C and corresponds to the loss of the free solvent Cl^- and ethanol molecules from the structure $([Ni_2HL_2(EtOH)_2](Cl)(EtOH))$ with TDTA = 118 °C. This loss represents about 9% of the complex mass. The second stage was recorded between 441 and 470 °C (TDTA = 451 °C) for the loss of 26% of the complex mass. This perdition is attributed to the loss of the two ethanol molecules and the decomposition of the ligand, as described above.

2.5. Dielectric Studies

The frequency dependence of the permittivity and the dielectric loss at room temperature of the ligand H_2L and the $[Ni_2HL_2(EtOH)_2](Cl)(EtOH)$ complex are illustrated in Figure 8. First, we observed that the dielectric parameters of the two samples show a plateau at high frequencies and then increase at low frequencies. The permittivity of the ligand H_2L is about 2.8, while its dissipation factor is 0.07 at high frequencies. The decrease in frequency leads to an increase in dielectric parameters until they reach 7.5 for ϵ_r and 0.55 for $\tan\delta$ at 1 Hz. It is well known that the dielectric parameters correspond to the polarization phenomenon in the materials. The observed increase in dielectric parameters at low frequencies can be due to space charge and defects in the material [42]. In other words, the applied electrical field helps in the jump of space charge and defects along low energy sites and their accumulation at high barrier energy sites results in an enhancement in the polarization at lower frequencies [43]. At higher frequencies, these charges cannot follow the oscillation of the electric field, leading to a decrease in ϵ_r . It worth noting that, for

a fixed frequency, one can observe that (i) the permittivity of the nickel(II) complex is lower than that of the free ligand H_2L and (ii) the dielectric loss of the complex is higher than that of the ligand. Thus, complexation of the ligand H_2L with Ni(II) results in a decrease in the permittivity and a slight increase in the dissipation factor. The decrease in the permittivity can be explained by the fact that the complexation reduces the space charge, defects, and electron density, which comes from the free nitrogen and oxygen atoms, of the H_2L ligand, in agreement with the above structure data, which showed that nitrogen and oxygen atoms are linked to nickel atoms in the nickel(II) complex.

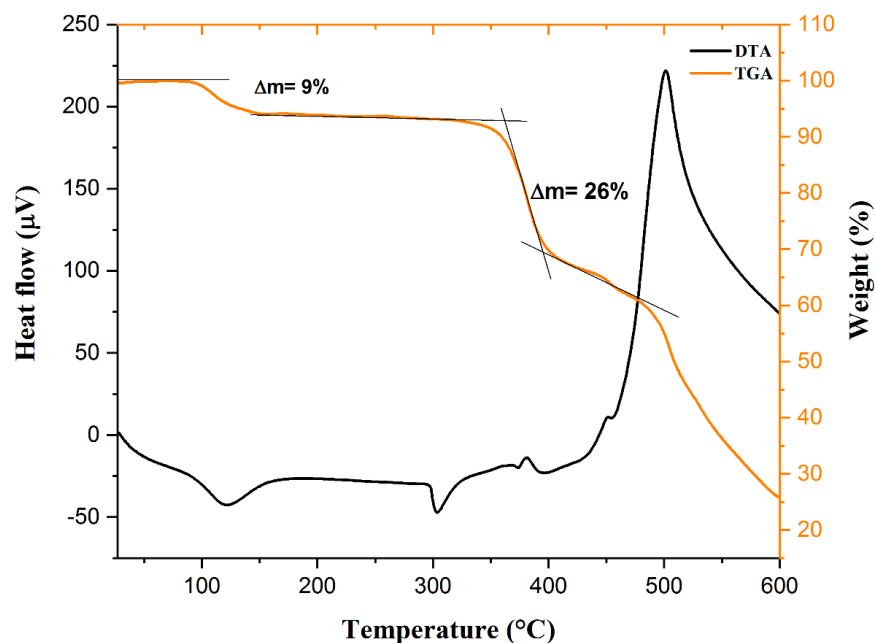


Figure 7. TGA and DTA of the $[Ni_2HL_2(EtOH)_2](Cl)(EtOH)$ complex.

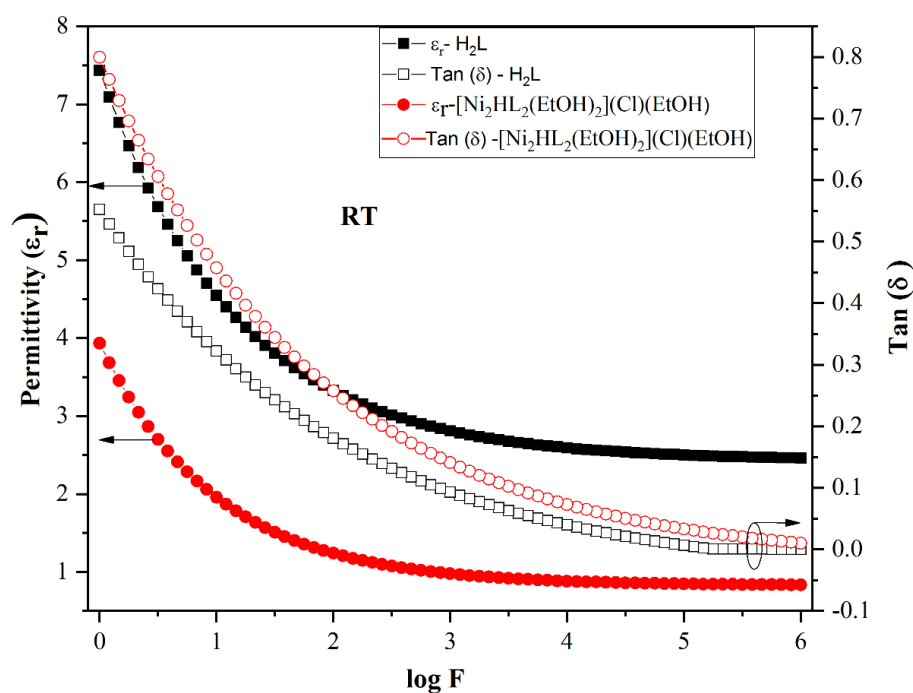


Figure 8. Frequency dependence of the permittivity (ϵ_r) and the dielectric loss $\tan(\delta)$ of H_2L and $[Ni_2HL_2(EtOH)_2](Cl)(EtOH)$ at room temperature.

The temperature dependence of the dielectric parameters ϵ_r and $\tan\delta$ of the studied compounds at 1 KHz are presented in Figure S4. It is found that the dielectric constant ϵ_r and the dielectric losses $\tan\delta$ increase slightly with temperature. An increase in the intensities of ϵ' and $\tan\delta$ at higher temperatures is apprehended on account of a reduction in bond energies in the materials. It seems that the orientation of small dipoles (polarons) and the electronic and ionic polarizations are facilitated with an increase in temperature.

2.6. Electrical Studies

2.6.1. Dc Electrical Conductivity

Figure S5a shows the Nyquist plot of the ligand H_2L measured at different temperatures and Figure S5b shows that of its corresponding nickel(II) complex. The extracted values of the dc conductivity (σ_{dc}) are tabulated in Table 2. From the analysis of the Nyquist plots, it is observed that the two samples present the same temperature behavior; the electrical resistance decreases by increasing temperature, suggesting that the electrical conductivity of the materials is thermally activated. The equivalent circuit of the conductivity in these samples can be described by a simple equivalent circuit of a parallel combination of a resistance R and a constant phase element (CPE). It is found, for each temperature, that the resistance of the ligand H_2L is lower than that of the bi-nuclear nickel complex, thereby the latter is more resistive.

Table 2. Room temperature values of the dielectric and electrical parameters for H_2L and the $[Ni_2HL_2(EtOH)_2](Cl)(EtOH)$ complex at 1 KHz.

Entry	ϵ_r	$\tan \delta$	$\sigma_{dc} \times 10^{-10}$ ($S \cdot cm^{-1}$)	$\sigma_{ac} \times 10^{-8}$ ($S \cdot cm^{-1}$)	E_a (eV)
H_2L	2.8	0.07	7.05	1.44	0.81
$[Ni_2HL_2(EtOH)_2](Cl)(EtOH)$	0.9	0.09	0.24	0.33	0.37

The electrical dc conductivity of each sample was calculated by the following Equation (1).

$$\sigma_{dc} = \frac{e}{S} \frac{1}{R} \quad (1)$$

where (e) is the thickness of the sample, (S) is the area of the sample–electrode contact, and (R) is the sample resistance at zero frequency (extracted from the Nyquist plot).

The variation in $\ln\sigma_{dc}$ as a function of $1000/T$ for H_2L and its nickel(II) complex is illustrated in Figure S6. It is found that the dc conductivity values throughout the temperature variation of H_2L are higher than those found for $[Ni_2HL_2(EtOH)_2](Cl)(EtOH)$. The ligand H_2L exhibits a dc conductivity of $7.05 \times 10^{-10} S \cdot cm^{-1}$ at RT and $1.94 \times 10^{-8} S \cdot cm^{-1}$ at 343 K, while its nickel(II) complex presents a dc conductivity of $2.40 \times 10^{-11} S \cdot cm^{-1}$ at RT and $1.57 \times 10^{-10} S \cdot cm^{-1}$ at 343 K. In addition, it is clearly observed that the dc conductivity increases linearly with the temperature for the two samples, which suggests that dc conductivity is a thermally activated process and follows an Arrhenius law defined as follows [44,45]:

$$\sigma_{dc} = \sigma_0 \exp(-E_a/K_B T) \quad (2)$$

where E_a is the activation energy, σ_0 is the pre-exponential factor, and K_B is the Boltzmann's constant. The activation energy values E_a were calculated using the slopes as shown in Figure S6. It is found that the ligand H_2L exhibits an activation energy of 0.81 eV, while the nickel(II) complexation has E_a equal to 0.37 eV. It appears that the complexation of the ligand reduces the activation energy of the conduction process. Therefore, the observed shrinking of the electrical conductivity in the complex is due to the reduction in the charge carriers.

2.6.2. Ac electrical Conductivity

The ac conductivity (σ_{ac}) of the under-study samples is calculated using the following equation:

$$\sigma_{tot} = (e/S) \cdot (Z' / Z'2 + Z''2) \quad (3)$$

The variation in ac conductivity ($\log \sigma_{ac}$) as a function of the frequency for H₂L and [Ni₂HL₂(EtOH)₂](Cl)(EtOH) recorded at room temperature is shown in Figure 9. It can be seen that the alternative conductivity increases linearly with frequency. This dispersion of the conductivity is in agreement with the expectation of Jonscher's power law [46]:

$$\sigma_{ac} = A\omega^s \quad (4)$$

where A is the pre-exponential factor, ω corresponds to $2\pi f$, and s (varies between 0 and 1) is the power-law exponent.

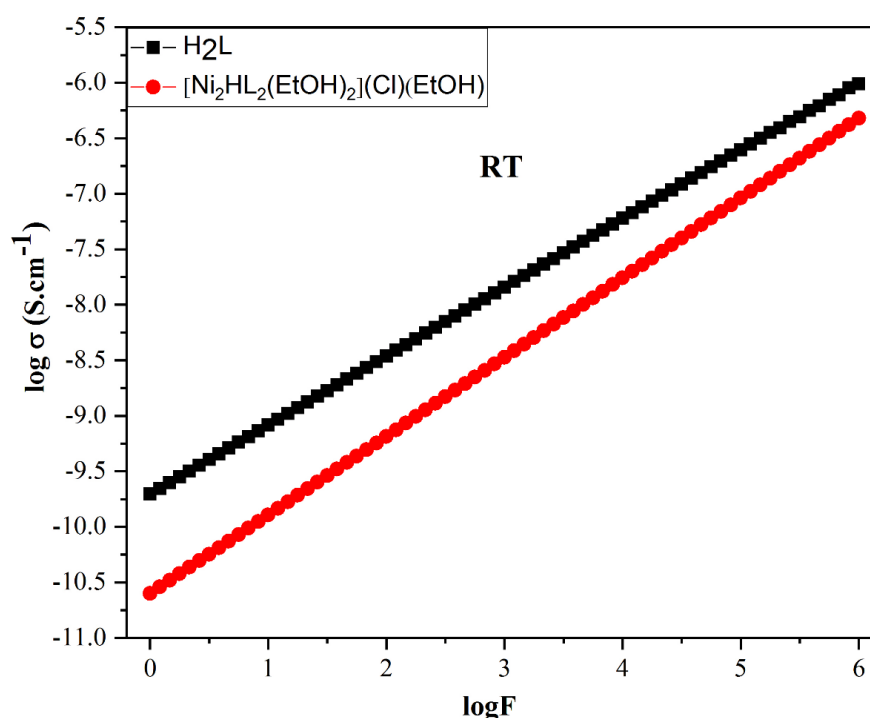


Figure 9. Frequency dependence of the conductivity ($\log \sigma_{ac}$) of H₂L and [Ni₂HL₂(EtOH)₂](Cl)(EtOH) at room temperature.

The variation in this parameter with temperature can provide information about the conduction mechanism in the samples. In fact, based on the variation in the frequency exponent with temperature, many mechanisms for the conduction are proposed [43,46]:

- If the frequency exponent (s) is independent of temperature, the mechanism is the quantum mechanical tunnel model (QMT);
- If (s) decreases to a minimum and then increases with a further increase in temperature, the mechanism is the large polaron tunnel model (LPT);
- If (s) increases with increasing temperature, the mechanism corresponds to the small polaron tunnel model (SPT);
- If (s) decreases with increasing temperature, the conductivity origin is described by the correlated barrier hopping (CBH) model.

The values of the frequency exponent (s) of the studied samples at different temperatures were determined from the linear plots at high frequencies, and its variation as a function of temperature is plotted in Figure S7. From the analysis of these spectra, it is found that the frequency exponent(s) decreases with increasing temperature. Thus, the

correlated barrier hopping (CBH) model is the appropriate mechanism to describe the conduction nature in the ligand H₂L and its nickel (II) complex. In this model, the charge carriers take place through the barriers separating the localized sites and the decrease in (s) values signifies a reduction in this energy barrier [47].

3. Materials and Methods

3.1. Experimental Section

All of the chemicals used in the experiment were obtained from Sigma-Aldrich, had an analytical grade, and were used as received with no further purification. The progress of the reactions was monitored by TLC and spots were visualized under UV light. The melting points were determined using a KOFER BENCH. The infrared spectra were recorded at room temperature using a BRUKER VERTEX 70 spectrometer. The ¹H and ¹³C NMR spectra were recorded at room temperature on a BRUKER AVANCE II 300 MHz instrument. The spin multiplicities are reported as singlet (s), doublet (d), triplet (t), multiplet (m), doublet of doublets (dd), doublet of triplets (dt), and quintet (qu). The high-resolution mass spectrum was recorded on a Waters/Vion IMS-QTOF: Spectrometer, equipped with an electrospray ionization (ESI) source, operating in either positive or negative ion mode. The electronic spectra were recorded in ethanol using a UV-6300PC/VWR spectrophotometer.

3.1.1. Preparation of Ligand H₂L

A mixture of propane-1,3-diamine (1.11 g, 14.97 mmol) and salicylaldehyde (3.66 g, 29.95 mmol) was refluxed in absolute ethanol (10 mL) until the consumption of reagents. The completion of the reaction was monitored by thin-layer chromatography (TLC). Then, the solvent was evaporated and the residue was crystallized in ethanol. The yellow precipitate was isolated by filtration and washed with cold ethanol and dried in vacuo. Yellow solid; yield: 3.97 g, 94%; m.p. = 112 °C; FT-IR: $\nu(\text{O-H})$: 3450 cm⁻¹, $\nu(\text{C=N})$: 1629 cm⁻¹, $\nu(\text{C=C})$: 1620 cm⁻¹, 1579 cm⁻¹, 1495 cm⁻¹, 1457 cm⁻¹, $\nu(\text{C-O})$: 1277 cm⁻¹; ¹H NMR (CDCl₃, 300 MHz) (δ , ppm): 2.13 (qu, 2H, CH₂, ³J = 6.6 Hz), 3.73 (t, 4H, ³J = 6.6 Hz), 6.91 (td, 2H, Ar-H, ⁴J_m = 1.2 Hz, ³J_o = 7.8 Hz), 7.00 (d, 2H, Ar-H, J = 8.4 Hz), 7.27 (dd, 2H, Ar-H, J_m = 1.8 Hz, J_o = 7.8 Hz), 7.34 (td, 2H, Ar-H, J_m = 1.5 Hz, J_o = 7.5 Hz), 8.39 (s, 2H, -CH=N), 13.47 (s, 2H, Ar-OH); ¹³C NMR (CDCl₃, 75 MHz) (δ , ppm): 31.72 (CH₂), 56.83 (CH₂-CH=N), 117.00, 118.66, 118.77 (-C_{Ar}-CH=N), 131.30, 132.30, 161.14 (-C_{Ar}-OH), 165.48 (-CH=N). UV/Vis in ethanol, λ_{max} nm [ϵ_{max} (L·mol⁻¹·cm⁻¹)]: 264 (32,567), 295 (12,943), 354 (4569), 440 (1344).

3.1.2. Synthesis and Crystallization of Nickel Complex [Ni₂HL₂(EtOH)₂](Cl)(EtOH)

To an ethanolic solution of the ligand H₂L (0.268 g, 0.95 mmol), a solution of NiCl₂ and 6H₂O (0.226 g, 0.95 mmol) in ethanol was added dropwise through a dropping funnel. Then, the mixture was refluxed for 4 h and left to cool to room temperature. The formed precipitate was isolated by filtration and washed with diethyl ether and cold ethanol. The obtained complex is insoluble in water, ether, chloroform, methylene chloride, and hexane. In contrast, it is soluble in methanol, ethanol, tetrahydrofuran, acetonitrile, dimethylformamide, and dimethyl sulfoxide. Therefore, it was recrystallized in ethanol and green crystals were obtained by slow evaporation of the ethanolic solution. Green crystals; yield: 0.648 g, 80%; m.p. > 260 °C; FT-IR (neat): $\nu(\text{C=N})$: 1610 cm⁻¹, $\nu(\text{C-O})$: 1192 cm⁻¹, $\nu(\text{Ni-O})$: 560 cm⁻¹, $\nu(\text{Ni-N})$: 444 cm⁻¹; UV/Vis in ethanol, λ_{max} nm [ϵ_{max} (L·mol⁻¹·cm⁻¹)]: 279 (16,062), 298 (14,139), 384(2419), 447(1827); ESI-QTOF-MS (*m/z*): mass calculated for [(Ni₂HL₂)(Cl)-H]⁺: 805.57555, found: 805.01499.

3.1.3. X-Ray Data Collection and Crystal Structure Determination

A single crystal of bi-nuclear nickel(II) complex derived from 2,2'-((propane-1,3-diylbis(azaneylylidene))bis(methaneylylidene))diphenol Schiff base was mounted on a Bruker D8 VENTURE four circles diffractometer equipped with a CCD bi-dimensional detector and INCOATEC I μ S micro-focus source MoK α monochromatic radiation

($\lambda = 0.71073 \text{ \AA}$) [48]. Data were corrected for Lorentz and polarization effects and for absorption [49]. The structure was solved by direct methods using SHELXT [50] and refined (by weighted full-matrix least-square on F2 techniques) to convergence using the SHELXL2016 program [33]. A summary of the measurement parameters is presented in Table 3. Hydrogen atoms were localized in a Fourier map or placed geometrically and included in the final cycles of refinement with isotropic thermal parameters, yielding the final R values summarized in Table 3. The final atomic coordinates and isotropic or equivalent isotropic displacement parameters are given in Table S1. The inter-atomic bond lengths and angles are summarized in Table S2. The hydrogen bonds O–H...Cl and the C–H... π interactions are reported in Table 4. The cif file containing the atomic positions, the anisotropic displacement parameters, the interatomic bonds and angles (supplement materials), and the measured and calculated intensities is deposited in the crystallographic Data Centre under the number CCDC 1904847. These data can be obtained free of charge via the Cambridge Crystallographic Data Centre, <https://www.ccdc.cam.ac.uk> (accessed on 30 August 2022), or e-mail: deposit@ccdc.cam.ac.uk.

Table 3. Crystal data, data collection, and structure refinement details for the $[\text{Ni}_2\text{HL}_2(\text{EtOH})_2](\text{Cl})(\text{EtOH})$ complex.

Crystal data	Chemical formula	$\text{C}_{38}\text{H}_{45}\text{N}_4\text{Ni}_2\text{O}_6 \cdot \text{C}_2\text{H}_6\text{O} \cdot \text{Cl}$
	M_r	852.71
	Crystal system, space group	Orthorhombic, $Pca2_1$
	Temperature (K)	296
	a, b, c (\AA)	17.5795 (12), 11.8562 (9), 20.2065 (13)
	V (\AA^3)	4211.6 (5)
	Z	4
	Radiation type	Mo $K\alpha$
	μ (mm^{-1})	1.01
Data collection	Crystal size (mm)	$0.36 \times 0.25 \times 0.18$
	Diffractometer	Bruker D8 VENTURE Super DUO [48]
	Absorption correction	Multi-scan [49]
	T_{\min}, T_{\max}	0.638, 0.746
	No. of measured, independent, and observed $[I > 2\sigma(I)]$ reflections	108,380, 10,452, 8643
	R_{int}	0.047
Refinement	$(\sin \theta / \lambda)_{\max}$ (\AA^{-1})	0.667
	$R[F^2 > 2\sigma(F^2)], wR(F^2), S$	0.029, 0.069, 1.01
	No. of reflections	10,452
	No. of parameters	517
	No. of restraints	59
	H-atom treatment	H atoms treated by a mixture of independent and constrained refinement
	$\Delta\rho_{\max}, \Delta\rho_{\min}$ (e \AA^{-3})	0.22, −0.22
	Absolute structure	Flack x determined using 3701 quotients $[(I^+) - (I^-)] / [(I^+) + (I^-)]$ [51]
	Absolute structure parameter	−0.002 (4)

Table 4. Hydrogen-bond geometry ($\text{\AA}, ^\circ$) for the $[\text{Ni}_2\text{HL}_2(\text{EtOH})_2](\text{Cl})(\text{EtOH})$ complex.

$D-H \dots A$	$D-H$	$H \dots A$	$D \dots A$	$D-H \dots A$
O5–H50...O1	0.82	1.66	2.401 (3)	148
O7–H7A...Cl1	0.82	2.28	3.060 (7)	160
O3–H3O...Cl1	0.86 (4)	2.24 (5)	3.082 (3)	165 (4)
O6–H6O...Cl1 ⁱ	0.86 (5)	2.25 (5)	3.102 (3)	171 (5)
C8–H8A...Cg11 ⁱⁱ	0.97	2.78	3.722 (4)	163
C10–H10A...Cg10	0.97	2.94	3.825 (4)	152
C19–H19A...Cg9	0.96	2.74	3.616 (5)	152

Symmetry code: (i) $x, y + 1, z$; (ii) $-1/2 + x, 1 - y, z$. Cg9: centroid of (C11–C16); Cg10: centroid of (C20–C25); Cg11: centroid of (C30–C35).

3.1.4. Electrical Measurements

The electrical measurements of the ligand H₂L and its corresponding nickel complex [Ni₂HL₂(EtOH)₂](Cl)(EtOH) were studied by impedance spectroscopy using a Modulab MTS data acquisition system equipped with a Linkam temperature control system. The powders of H₂L and [Ni₂HL₂(EtOH)₂](Cl)(EtOH) were pressed to form pellets of 1 mm in thickness and 10 mm in diameter. Then, the pellets were electroded with silver lacquer and placed in the Linkam-type sample holder. The conductance and capacitance measurements were collected at different frequencies (1 Hz–1 MHz) in the temperature range from room temperature (RT) to 343 K. From the collected data, the dielectric parameters (permittivity (ϵ_r) and dielectric loss (Tan (δ))) and the electrical parameters (dc and ac conductivity and activation energy (E_a)) were determined.

4. Conclusions

In summary, we prepared a new bi-nuclear nickel complex based on 2,2'-((propane-1,3-diylbis(azaneylylidene))bis(methaneylylidene))diphenol Schiff base. The structures were evidenced without doubt through spectroscopic and single crystal X-ray diffraction analysis, which showed that the chelation occurs through the deprotonated phenolic oxygen and azomethine nitrogen atoms of the ligand. The coordination behavior shown for the H₂L ligand, in this case, is totally different from that shown in previously published work. Hirshfeld surface analysis was performed to explore the intermolecular interactions and packing patterns in the crystal structure. The electrical conductivity of the H₂L ligand is diminished with nickel(II) coordination. The complex [Ni₂HL₂(EtOH)₂](Cl)(EtOH) exhibits a dc conductivity of $2.40 \times 10^{-11} \text{ S}\cdot\text{cm}^{-1}$ at room temperature, which indicates the electrical insulating nature of this complex. The frequency dependence of the conductivity showed that the conductivity of both compounds follows Jonscher's universal power law. The variation in the frequency exponent (s) with temperature demonstrates that the conduction nature in the samples is described by the correlated barrier hopping (CBH) mechanism.

Supplementary Materials: The following supporting information can be downloaded at: <https://www.mdpi.com/article/10.3390/chemistry4040080/s1>, Figure S1: FT-IR spectrum of the ligand H₂L; Figure S2: FT-IR spectrum of the [Ni₂HL₂(EtOH)₂](Cl)(EtOH) complex; Figure S3: Mass spectrum of the [Ni₂HL₂(EtOH)₂](Cl)(EtOH) complex; Figure S4: Temperature dependence of the permittivity (ϵ_r) and the dielectric loss tan (δ) of H₂L and [Ni₂HL₂(EtOH)₂](Cl)(EtOH) at 1KHz; Figure S5: Cole-Cole diagrams of (a) H₂L and (b) [Ni₂HL₂(EtOH)₂](Cl)(EtOH) at different temperatures; Figure S6: ln (σ_{dc}) versus $10^3/T$ plots of H₂L and [Ni₂HL₂(EtOH)₂](Cl)(EtOH); Figure S7: Temperature dependence of the exponent (s) of H₂L and [Ni₂HL₂(EtOH)₂](Cl)(EtOH); Table S1: Fractional atomic coordinates and isotropic or equivalent isotropic displacement parameters (\AA^2) of [Ni₂HL₂(EtOH)₂](Cl)(EtOH) complex; Table S2: Atomic displacement parameters (\AA^2) for [Ni₂HL₂(EtOH)₂](Cl)(EtOH) complex; Table S3: Selected bond distances (\AA) and angles ($^\circ$) for the [Ni₂HL₂(EtOH)₂](Cl)(EtOH) complex.

Author Contributions: Experiments; writing—original draft preparation, B.E.-S.; crystallographic studies, M.S., L.E.A., L.B. (Linda Bejaoui) and S.K.; electrical studies, E.M.H. and L.B. (Lahcen Bih); spectroscopic analysis, M.E.Y. and A.N.; writing—review and editing, M.B., L.B. (Linda Bejaoui) and S.K; methodology; supervision, M.F. All authors have read and agreed to the published version of the manuscript.

Funding: This research received no external funding.

Data Availability Statement: Not applicable.

Acknowledgments: The authors thank the Faculty of Science, Mohammed V University in Rabat, Morocco for the X-ray measurements; City of Innovation, Sidi Mohamed Ben Abdallah University of Fez, Morocco for spectroscopic accomplishments.

Conflicts of Interest: The authors declare no conflict of interest.

References

1. Abdel-Rahman, L.H.; Ismail, N.M.; Ismael, M.; Abu-Dief, A.M.; Ahmed, E.A.-H. Synthesis, Characterization, DFT Calculations and Biological Studies of Mn(II), Fe(II), Co(II) and Cd(II) Complexes Based on a Tetradentate ONNO Donor Schiff Base Ligand. *J. Mol. Struct.* **2017**, *1134*, 851–862. [\[CrossRef\]](#)
2. Kargar, H.; Fallah-Mehrjardi, M.; Behjatmanesh-Ardakani, R.; Bahadori, M.; Moghadam, M.; Ashfaq, M.; Munawar, K.S.; Tahir, M.N. Pd(II) and Ni(II) Complexes Containing ONNO Tetradentate Schiff Base Ligand: Synthesis, Crystal Structure, Spectral Characterization, Theoretical Studies, and Use of PdL as an Efficient Homogeneous Catalyst for Suzuki–Miyaura Cross-Coupling Reaction. *Polyhedron* **2022**, *213*, 115622. [\[CrossRef\]](#)
3. Hajjaji, F.E.; Belghiti, M.E.; Drissi, M.; Fahim, M.; Salim, R.; Hammouti, B.; Taleb, M.; Nahle, A. Electrochemical, Quantum Calculations and Monte Carlo Simulation Studies of N1, N2-Bis (1-Phenylethylidene) Ethane-1, 2-Diamine as a Corrosion Inhibitor for Carbon Steel in a 1.0 M Hydrochloric Acid Solution. *Port. Electrochim. Acta* **2019**, *37*, 23–42. [\[CrossRef\]](#)
4. Bahron, H.; Ahmad, S.N.; Tajuddin, A.M. Substituent Effect on Catalytic Activity of Palladium(II) Schiff Base Complexes for Sonogashira Reaction. *J. Sci. Technol.* **2017**, *11*, 115–124.
5. Al Zoubi, W.; Ko, Y.G. Schiff Base Complexes and Their Versatile Applications as Catalysts in Oxidation of Organic Compounds: Part I. *Appl. Organomet. Chem.* **2017**, *31*, e3574. [\[CrossRef\]](#)
6. Trujillo, A.; Fuentealba, M.; Carrillo, D.; Manzur, C.; Ledoux-Rak, I.; Hamon, J.-R.; Saillard, J.-Y. Synthesis, Spectral, Structural, Second-Order Nonlinear Optical Properties and Theoretical Studies On New Organometallic Donor–Acceptor Substituted Nickel(II) and Copper(II) Unsymmetrical Schiff-Base Complexes. *Inorg. Chem.* **2010**, *49*, 2750–2764. [\[CrossRef\]](#) [\[PubMed\]](#)
7. Wesley Jeevadason, A.; Kalidasa Murugavel, K.; Neelakantan, M.A. Review on Schiff Bases and Their Metal Complexes as Organic Photovoltaic Materials. *Renew. Sustain. Energy Rev.* **2014**, *36*, 220–227. [\[CrossRef\]](#)
8. Ahmed, A.H.; Moustafa, M.G. Spectroscopic, Morphology and Electrical Conductivity Studies on Co(II), Ni(II), Cu(II) and Mn(II)-Oxaloyldihydrazone Complexes. *J. Saudi Chem. Soc.* **2020**, *24*, 381–392. [\[CrossRef\]](#)
9. Sarkar, S.; Biswas, S.; Liao, M.-S.; Kar, T.; Aydogdu, Y.; Dagdelen, F.; Mostafa, G.; Chattopadhyay, A.P.; Yap, G.P.A.; Xie, R.-H.; et al. An Attempt towards Coordination Supramolecularity from Mn(II), Ni(II) and Cd(II) with a New Hexadentate [N₄O₂] Symmetrical Schiff Base Ligand: Syntheses, Crystal Structures, Electrical Conductivity and Optical Properties. *Polyhedron* **2008**, *27*, 3359–3370. [\[CrossRef\]](#)
10. Li, L.-F.; Zhang, L.; Xu, Y.; Zhu, L.-L.; Yang, P.-P. Synthesis, Crystal Structure, and Magnetic Properties of a Series of Binuclear Lanthanide Compounds Derived from the 4-Bromo-2-((Quinolin-8-Ylimino)Methyl)Phenol Ligand. *Inorg. Chim. Acta* **2018**, *482*, 779–784. [\[CrossRef\]](#)
11. Banerjee, S.; Drew, M.G.B.; Lu, C.-Z.; Tercero, J.; Diaz, C.; Ghosh, A. Dinuclear Complexes of MII Thiocyanate (M = Ni and Cu) Containing a Tridentate Schiff-Base Ligand: Synthesis, Structural Diversity and Magnetic Properties. *Eur. J. Inorg. Chem.* **2005**, *2005*, 2376–2383. [\[CrossRef\]](#)
12. Arunadevi, A.; Raman, N. Biological Response of Schiff Base Metal Complexes Incorporating Amino Acids—A Short Review. *J. Coord. Chem.* **2020**, *73*, 2095–2116. [\[CrossRef\]](#)
13. Uddin, M.N.; Ahmed, S.S.; Alam, S.M.R. REVIEW: Biomedical Applications of Schiff Base Metal Complexes. *J. Coord. Chem.* **2020**, *73*, 3109–3149. [\[CrossRef\]](#)
14. Ayad, M.I.; Ayad, M.M. Electrical Properties of Ga(III), In(III), Zr(IV) and Sn(IV) Complexes with Schiff Bases Derived from 2-Hydroxynaphthaldehyde and Phenylenediamines. *J. Mater. Sci. Mater. Electron.* **1993**, *4*, 125–128. [\[CrossRef\]](#)
15. Alkhatib, F.; Hameed, A.; Sayqal, A.; Bayazeed, A.A.; Alzahrani, S.; Al-Ahmed, Z.A.; Althagafi, I.; Zaky, R.; El-Metwaly, N.M. Green-Synthesis and Characterization for New Schiff-Base Complexes; Spectroscopy, Conductometry, Hirshfeld Properties and Biological Assay Enhanced by in-Silico Study. *Arab. J. Chem.* **2020**, *13*, 6327–6340. [\[CrossRef\]](#)
16. De Domingo, E.; Folcia, C.L.; Ortega, J.; Etxebarria, J.; Termine, R.; Goleme, A.; Coco, S.; Espinet, P. Striking Increase in Hole Mobility upon Metal Coordination to Triphenylene Schiff Base Semiconducting Multicolumnar Mesophases. *Inorg. Chem.* **2020**, *59*, 10482–10491. [\[CrossRef\]](#)
17. Shebl, M. Synthesis, Spectral and Magnetic Studies of Mono- and Bi-Nuclear Metal Complexes of a New Bis(Tridentate NO₂) Schiff Base Ligand Derived from 4,6-Diacetylresorcinol and Ethanolamine. *Spectrochim. Acta Part A Mol. Biomol. Spectrosc.* **2009**, *73*, 313–323. [\[CrossRef\]](#)
18. Goswami, S.; Singha, S.; Saha, R.; Singha Roy, A.; Islam, M.; Kumar, S. A Bi-Nuclear Cu(II)-Complex for Selective Epoxidation of Alkenes: Crystal Structure, Thermal, Photoluminescence and Cyclic Voltammetry. *Inorg. Chim. Acta* **2019**, *486*, 352–360. [\[CrossRef\]](#)
19. Ghorai, P.; Brandão, P.; Benmansour, S.; García, C.J.G.; Saha, A. Azido and Thiocyanato Bridged Dinuclear Ni(II) Complexes Involving 8-Aminoquinoline Based Schiff Base as Blocking Ligands: Crystal Structures, Ferromagnetic Properties and Magneto-Structural Correlations. *Polyhedron* **2020**, *188*, 114708. [\[CrossRef\]](#)
20. Bhowmik, P.; Chattopadhyay, S.; Drew, M.G.B.; Diaz, C.; Ghosh, A. Synthesis, Structure and Magnetic Properties of Mono- and Di-Nuclear Nickel(II) Thiocyanate Complexes with Tridentate N₃ Donor Schiff Bases. *Polyhedron* **2010**, *29*, 2637–2642. [\[CrossRef\]](#)
21. Matsunaga, S.; Shibasaki, M. Recent Advances in Cooperative Bimetallic Asymmetric Catalysis: Dinuclear Schiff Base Complexes. *Chem. Commun.* **2014**, *50*, 1044–1057. [\[CrossRef\]](#) [\[PubMed\]](#)
22. Mitsunuma, H.; Matsunaga, S. Dinuclear Ni 2—Schiff Base Complex-Catalyzed Asymmetric 1,4-Addition of β -Keto Esters to Nitroethylene toward γ 2,2 -Amino Acid Synthesis. *Chem. Commun.* **2011**, *47*, 469–471. [\[CrossRef\]](#) [\[PubMed\]](#)

23. Cheng, H.; Wang, H.; Li, Y.; Hu, Y.; Zhang, X.; Cai, Z. Structurally Simple Dinuclear Nickel Catalyzed Olefin Copolymerization with Polar Monomers. *J. Catal.* **2018**, *368*, 291–297. [\[CrossRef\]](#)
24. Takeuchi, D. Olefin Polymerization and Copolymerization Catalyzed by Dinuclear Catalysts Having Macrocyclic Ligands. *J. Synth. Org. Chem. Jpn.* **2019**, *77*, 1136–1146. [\[CrossRef\]](#)
25. Anbu, S.; Kandaswamy, M.; Varghese, B. Structural, Electrochemical, Phosphate-Hydrolysis, DNA Binding and Cleavage Studies of New Macrocyclic Binuclear Nickel(II) Complexes. *Dalton Trans.* **2010**, *39*, 3823–3832. [\[CrossRef\]](#) [\[PubMed\]](#)
26. Hamaguchi, T.; Kai, K.; Ando, I.; Kawano, K.; Yamauchi, K.; Sakai, K. A Dinuclear Nickel Catalyst Based on Metal–Metal Cooperation for Electrochemical Hydrogen Production. *Inorg. Chim. Acta* **2020**, *505*, 119498. [\[CrossRef\]](#)
27. Xu, W.; Li, M.; Qiao, L.; Xie, J. Recent Advances of Dinuclear Nickel- and Palladium-Complexes in Homogeneous Catalysis. *Chem. Commun.* **2020**, *56*, 8524–8536. [\[CrossRef\]](#)
28. Azam, M.; Al-Resayes, S.I.; Soliman, S.M.; Trzesowska-Kruszynska, A.; Kruszynski, R.; Khan, Z. A (Salicylaldiminato)Pt(II) Complex with Dimethylpropylene Linkage: Synthesis, Structural Characterization and Antineoplastic Activity. *J. Photochem. Photobiol. B Biol.* **2017**, *176*, 150–156. [\[CrossRef\]](#)
29. Azam, M.; Al-Resayes, S.I. Phenoxy-Bridged Binuclear Zn(II) Complex Holding Salen Ligand: Synthesis and Structural Characterization. *J. Mol. Struct.* **2016**, *1107*, 77–81. [\[CrossRef\]](#)
30. Shelar, M.D.; Quadri, S.; Pathan, M.A.A.K.; Kamble, S.; Farooqui, M.; Nuzaat, D.A.; Shaikh, J.D.; Syed, F.M. Pharmaceutically Fine Synthesis and Their Study of Antimicrobial Activity of Metal Complexes with Some Schiff's Bases. *Der Pharma Chem.* **2011**, *3*, 486–490.
31. Corden, J.P.; Errington, W.; Moore, P.; Wallbridge, M.G.H. N,N'-Bis(2-Hydroxybenzylidene)-2,2-Dimethyl-1,3-Propanediamine. *Acta Cryst. C* **1996**, *52*, 125–127. [\[CrossRef\]](#)
32. Farrugia, L.J. WinGX and ORTEP for Windows: An Update. *J. Appl. Cryst.* **2012**, *45*, 849–854. [\[CrossRef\]](#)
33. Sheldrick, G.M. Crystal Structure Refinement with SHELXL. *Acta Cryst. C* **2015**, *71*, 3–8. [\[CrossRef\]](#) [\[PubMed\]](#)
34. Spek, A.L. PLATON SQUEEZE: A Tool for the Calculation of the Disordered Solvent Contribution to the Calculated Structure Factors. *Acta Cryst. C* **2015**, *71*, 9–18. [\[CrossRef\]](#)
35. You, Z.-L.; Qiu, X.-Y.; Xian, D.-M.; Zhang, M. Unprecedented Preparation of Dinuclear Nickel(II) and Zinc(II) Complexes with Schiff Base Ligands Transformation Under Solvothermal Conditions. *Inorg. Chem. Commun.* **2012**, *26*, 11–16. [\[CrossRef\]](#)
36. Fondo, M.; Doejo, J.; Garcia-Deibe, A.M.; Ocampo, N.; Sanmartin, J. Carboxylic Decorated Schiff Base Complexes as Metallotectons for Hydrogen Bonded 3D Networks. *Polyhedron* **2015**, *101*, 78–85. [\[CrossRef\]](#)
37. Mahapatra, P.; Bauza, A.; Frontera, A.; Drew, M.G.B.; Ghosh, A. Syntheses of Four New Asymmetric Schiff Bases and Their Cu(II) Complexes: Theoretical calculations to rationalize the packing of molecules in the crystals. *Inorg. Chim. Acta* **2018**, *477*, 89–101. [\[CrossRef\]](#)
38. Aragón-Muriel, A.; Reyes-Márquez, V.; Cañavera-Buelvas, F.; Parra-Unda, J.R.; Cuenú-Cabezas, F.; Polo-Cerón, D.; Colorado-Peralta, R.; Suárez-Moreno, G.V.; Aguilar-Castillo, B.A.; Morales-Morales, D. Pincer Complexes Derived from Tridentate Schiff Bases for Their Use as Antimicrobial Metallopharmaceuticals. *Inorganics* **2022**, *10*, 134. [\[CrossRef\]](#)
39. Jayamani, A.; Nagasubramanian, S.; Thamilarasan, V.; Ojwach, S.O.; Gopu, G.; Sengottuvelan, N. In-Situ Nickel(II) Complexes of 3-(Dimethylamino)-1-Propylamine Based Schiff Base Ligands: Structural, Electrochemical, Biomolecular Interaction and Antimicrobial Properties. *Inorg. Chim. Acta* **2018**, *482*, 791–799. [\[CrossRef\]](#)
40. Tadavi, S.K.; Rajput, J.D.; Bagul, S.D.; Hosamani, A.A.; Sangshetti, J.N.; Bendre, R.S. Synthesis, Crystal Structures, Biological Screening and Electrochemical Analysis of Some Salen-Based Transition Metal Complexes. *Res. Chem. Intermed.* **2017**, *43*, 4863–4879. [\[CrossRef\]](#)
41. Jayamani, A.; Sethupathi, M.; Ojwach, S.O.; Sengottuvelan, N. Investigation on Biomolecular Interactions of Nickel(II) Complexes with Monoanionic Bidentate Ligands. *J. Mol. Struct.* **2018**, *1151*, 6–16. [\[CrossRef\]](#)
42. Morgan, S.M.; El-Ghamaz, N.A.; Diab, M.A. Effect of the Type of Metal on the Electrical Conductivity and Thermal Properties of Metal Complexes: The Relation between Ionic Radius of Metal Complexes and Electrical Conductivity. *J. Mol. Struct.* **2018**, *1160*, 227–241. [\[CrossRef\]](#)
43. Hassib, H.; Abdel Razik, A. Dielectric Properties and AC Conduction Mechanism for 5,7-Dihydroxy-6-Formyl-2-Methylbenzo-Pyran-4-One Bis-Schiff Base. *Solid State Commun.* **2008**, *147*, 345–349. [\[CrossRef\]](#)
44. Laajimi, M.; Jebnoui, A.; Chemli, M.; Majdoub, M.; Ben Chaabane, R. Optical, Dielectric and Oxygen Sensing Properties of an Anthracene and Carbazole Based π -Conjugated Schiff Base. *Mater. Chem. Phys.* **2019**, *228*, 336–343. [\[CrossRef\]](#)
45. El-Ghamaz, N.A.; El-Sonbati, A.Z.; Diab, M.A.; El-Bindary, A.A.; Awad, M.K.; Morgan, S.M. Dielectrical, Conduction Mechanism and Thermal Properties of Rhodanine Azodyes. *Mater. Sci. Semicond. Process.* **2014**, *19*, 150–162. [\[CrossRef\]](#)
46. Jonscher, A.K. Dielectric Relaxation in Solids. *J. Phys. D Appl. Phys.* **1999**, *32*, R57–R70. [\[CrossRef\]](#)
47. El-Ghamaz, N.A.; El-Bindary, A.A.; Diab, M.A.; El-Sonbati, A.Z.; Nozha, S.G. Dielectrical Properties and Conduction Mechanism of Quinoline Schiff Base and Its Complexes. *Res. Chem. Intermed.* **2016**, *42*, 2501–2523. [\[CrossRef\]](#)
48. Bruker. APEX3 (Version 5.054), SAINT+ (Version 6.36A), SADABS; Bruker AXS Inc.: Madison, WI, USA, 2016.
49. Krause, L.; Herbst-Irmer, R.; Sheldrick, G.M.; Stalke, D. Comparison of Silver and Molybdenum Microfocus X-Ray Sources for Single-Crystal Structure Determination. *J. Appl. Cryst.* **2015**, *48*, 3–10. [\[CrossRef\]](#)

-
50. Sheldrick, G.M. SHELXT—Integrated Space-Group and Crystal-Structure Determination. *Acta Cryst. A* **2015**, *71*, 3–8. [[CrossRef](#)]
 51. Parsons, S.; Flack, H.D.; Wagner, T. Use of Intensity Quotients and Differences in Absolute Structure Refinement. *Acta Cryst. B* **2013**, *69*, 249–259. [[CrossRef](#)]